

Time scales and spatial patterns of passive ocean-atmosphere decay modes

BENJAMIN R. LINTNER

*Department of Atmospheric Sciences, and Institute of Geophysics and Planetary Physics, University of
California, Los Angeles*

J. DAVID NEELIN

*Department of Atmospheric Sciences, and Institute of Geophysics and Planetary Physics, University of
California, Los Angeles*

Corresponding author address: *Dr. Benjamin R. Lintner, Department of Atmospheric Sciences, University
of California, Los Angeles, Los Angeles, 405 Hilgard Ave., 7127 Math Science Bldg., Los Angeles, CA
90095-1565. E-mail: ben@atmos.ucla.edu*

A version in AMS preprint format may be obtained at
<http://www.atmos.ucla.edu/~csi/REF/pdfs/sstdecay.pdf>

Submitted February 20th, 2007

Abstract

The decay characteristics of a mixed layer ocean passively coupled to an atmospheric model are important to the response of the climate system to stochastic or external forcing. We address here two salient features of such decay: the scale dependence of sea surface temperature anomaly (SSTA) decay timescales and the spatial inhomogeneities of SSTA decay modes. As expected, decay timescales increase with the spatial extent of the SSTA. Most modes decay rapidly—with characteristic decay times of 50-100 days for a 50 m mixed layer—with the decay determined by local surface flux adjustment. Only those modes with spatial scales approaching or larger than the tropical basin scale exhibit decay timescales distinctively longer than the local decay, with the decay timescale of the most slowly decaying mode of order 250-300 days in the tropics (500 days globally). Simple analytic prototypes of the spatial scale dependence and the effect of basic state inhomogeneities, especially the impact of nonconvecting regions, elucidate these results. Horizontal energy transport sets the transition between the fast, essentially local, decay timescales and the slower decay at larger spatial scales; within the Tropics, efficient wave dynamics account for the small number of slowly-decaying modes. Inhomogeneities in the basic state climate, such as the presence or absence of mean tropical deep convection, strongly impact large-scale SSTA decay characteristics. For nonconvecting regions, SSTA decay is slow because evaporation is limited by relatively slow moisture divergence. The separation of convecting and nonconvecting region decay times and the closeness of the slower nonconvecting region decay timescale to the most slowly-decaying modes cause a blending of properties between local nonconvecting modes and the large-scale modes, resulting in strong spatial inhomogeneity in the slow decay modes.

1. Introduction

Coupling of the ocean-atmosphere system is an important facet of climate system variability relevant to adjustment processes and teleconnections. It is conceptually useful to distinguish two types of ocean-atmosphere coupling: “active” and “passive.” The former involves changes to ocean circulation, e.g., surface windstress forcing or thermocline dynamics, that impact SST and feedback to the atmosphere. Active coupling plays a crucial role in the evolution and dynamics of the El Niño/Southern Oscillation (ENSO; Philander et al 1984; Cane and Zebiak, 1986; Battisti, 1988; Neelin et al 1998 and references therein), as interactions of the thermocline, ocean wave dynamics, surface fluxes, and convection dictate the spatial extent and timescales of ENSO events. Active coupling has been further implicated in the low frequency variability of the extratropical SSTAs, with oceanic Rossby wave dynamics and the thermohaline and wind-driven circulations contributing to the development of spatially coherent modes of SSTA variability on interdecadal and longer timescales (Munnich et al 1998; Neelin and Weng 1999; Gallego and Cessi 2001; Marshall et al 2001).

Passive ocean-atmosphere coupling is simpler, as it involves only thermodynamically-mediated changes to ocean heat storage. The use of passive coupling is well known from studies of the extratropical SST response to high-frequency atmospheric forcing (Hasselmann, 1976; Frankignoul and Hasselmann, 1977; Barsugli and Battisti, 1997). For reference, the simplest stochastic model of mixed layer surface temperature T_s via atmospheric forcing F (Hasselmann 1976; Frankignoul and Hasselmann 1977) is

$$c_M \partial_t T_s = -\lambda_{T_s} T_s + F \quad (1)$$

where c_M is the mixed layer heat capacity and λ_{T_s} is a damping coefficient representing the net surface heat flux anomaly per T_s anomaly.

Within the tropics, passive coupling also plays a significant role, especially in the context of

tropical teleconnections (Klein et al., 1999; Saravanan and Chang, 2000). The thermal inertia of the ocean mixed layer delays the remote surface temperature response to El Niño, which in turn impacts tropospheric warming and precipitation (see, e.g., Chang, 1998; Alexander et al., 2001; Giannini et al., 2001; Chiang and Sobel, 2002; Tang and Neelin, 2004; Neelin and Su, 2005; Su and Neelin, 2005, hereafter SN05; Chiang and Lintner, 2005). Studies of other coupled tropical phenomena, including intraseasonal variability and the Madden-Julian Oscillation, further demonstrate the potential impacts of passive coupling (Sobel and Gildor, 2003; Maloney and Sobel, 2004; Grabowski, 2006; Zhang et al., 2006).

SN05 developed a simple, passively coupled tropical ocean-atmosphere analogue to the Hasselmann model (1) with tropospheric temperature T representing the state of the tropical atmosphere:

$$c_M \partial_t T_s = -\lambda_{T_s} T_s + \lambda_{SFC} T \quad (2)$$

$$c_A \partial_t T = -[\lambda_{TOA} + \lambda_{EXPORT} + (1 - \sigma_L) \lambda_{SFC}] T + \lambda_{T_s} T_s \quad (3)$$

Here, c_M is as in equation (1); c_A is tropospheric heat capacity; λ_{SFC} , λ_{TOA} , and λ_{EXPORT} are damping coefficients for atmospheric heat flux anomalies (per unit T anomaly) across the ocean surface, the top of the atmosphere (TOA), and approximate transports to the extratropics, respectively; and σ_L is the fraction of land area. The damping coefficient λ_{T_s} is defined slightly differently than in (1): here it represents the net surface flux anomaly per T_s when atmospheric T is fixed.

Equations (2) and (3) are characterized by uncoupled decay timescales $c_M \lambda_{T_s}^{-1}$ and $c_A [\lambda_{TOA} + \lambda_{EXPORT} + (1 - \sigma_L) \lambda_{SFC}]^{-1}$ for the ocean and atmosphere components, respectively. On the other hand, the slow *coupled* decay timescale of the tropical ocean-atmosphere system, on the scale of the entire tropics,

$$\tau_G = c_M \lambda_{T_s}^{-1} [1 + (1 - \sigma_L) \lambda_{SFC} (\lambda_{TOA} + \lambda_{EXPORT})^{-1}] \quad (4)$$

is longer than the uncoupled decay timescales of either the atmospheric or oceanic components.

For reference, SN05 estimated a value for τ_g of roughly 260 days for a 50 m mixed layer.

In a strict sense, the SN05 model applies only to coupled mode decay for tropical mean conditions, and in section 5, we consider a local extension to (4). However, we can anticipate some of the effects encountered in the local analogue of (4). Since the tropical basic state climate is spatially inhomogeneous, locally estimated damping timescales may deviate substantially from the tropical mean value: regional differences in the damping, exchange, and feedback coefficients (e.g., turbulent flux windspeed dependences) may lead to pronounced regional differences in local decay times. Park et al. (2005) estimated the surface heat flux response to SSTAs and found regional differences of order 25 Wm^{-2} , although intratropical differences tend to be smaller. Inhomogeneities in ocean mixed-layer depth also impact regional decay characteristics, as mixed-layer depth varies over an order of magnitude both geographically and seasonally (Kara et al., 2003).

The spatial scale dependence of decay timescales complicates the study of passive ocean-atmosphere coupling. Previous studies (e.g., Bretherton, 1982; Frankignoul, 1985; Schopf, 1985; Marotzke and Pierce, 1997; Nilsson, 2000; SN05) considered the effect of anomaly size on SSTA decay characteristics and identified decay regimes set by physics at various scales. For sufficiently localized anomalies, decay times are set by local surface exchange coefficients; at the largest scales, by contrast, decay is limited by top-of-the-atmosphere outgoing longwave radiation. Since a key aspect in the transition between scales is the efficiency of net energy export away from an anomaly, equation (4) is again instructive. The λ_{EXPORT} term approximates horizontal energy flux (per T) across a domain boundary, divided by the area of the domain. For a sufficiently localized SSTA, atmospheric heat transport away from the anomaly is large compared to the vertical export over the area of the anomaly, so $\lambda_{EXPORT} \gg \lambda_{SFC}$; from (4), this implies decay on a timescale comparable to an *uncoupled* mixed layer. On the other hand, as the size of the SSTA increases, the efficiency of heat transport is diminished; in the limit $\lambda_{EXPORT} \ll \lambda_{TOA}$, the decay timescale is (setting $\sigma_L = 0$ for simplicity) $\tau_G = c_M \lambda_{SST}^{-1} [1 + \lambda_{SFC} \lambda_{TOA}^{-1}]$. Since λ_{TOA} is small compared to λ_{SFC} , and $\lambda_{SFC} / \lambda_{SST}$ is $O(1)$, the decay of large-scale SSTAs is slow rel-

ative to more localized anomalies. While this simple picture contains much that is correct, the explicit inclusion of local physics, especially moist dynamics, has nontrivial consequences. In the Tropics, horizontal transports are accomplished largely by planetary wave dynamics, with local tropospheric warming driven primarily by moist convection and remote warming occurring through compensating descent. The ascending and descending circulations interact with the tropospheric moisture field, which (as we will see below) has significant consequences for the decay characteristics of convecting and nonconvecting regions.

Given the relevance of passive ocean-atmosphere coupling to climate variability, our interest here is to develop a general framework for understanding the spatial structure of passively coupled tropical ocean-atmosphere decay modes as well as the decay time spatial scale dependence of these modes. An obvious caveat is that the absence of ocean dynamics means that some potentially important physical mechanisms are lacking. However, we argue that the passive coupling framework is a highly useful (and nontrivial) starting point, worth establishing in its own right, especially as an aid to understanding the interaction of these modes with active coupling phenomena such as ENSO.

2. Autocorrelation function persistence analysis

Temporal autocorrelation functions have been widely used to infer the persistence/decay characteristics of observed mid- and high-latitude SSTAs (see, for example, Bhatt et al., 1998; Kushnir, 2000; Watanabe and Kimoto, 2002; Timlin et al., 2002; Deser et al., 2003). These studies suggest characteristic damping timescales for extratropical SSTAs of order 90-180 days. Longer persistence values have been noted, e.g., seasonal changes in mixed layer depth as well as subsurface dynamics (e.g., the reemergence mechanism) can impact the decay times.

To motivate the present analysis, we apply autocorrelation persistence to SSTAs as simulated by a passive ocean mixed layer of constant 50 m depth coupled to an atmospheric intermediate level complexity model, the Quasi-equilibrium Tropical Circulation Model 1 version 2.3 (here-

after, QTCM1; see Neelin and Zeng, 2000; Zeng et al., 2000), and a general circulation model, the NCAR Community Climate Model version 3.10 (hereafter, CCM3; see Kiehl et al., 1998). For QTCM1, the output consists of 10 independent simulations, each of 50 years duration and at a longitude-latitude resolution of $5.625^\circ \times 3.75^\circ$. The CCM3 output consists of a single, 85 year integration at T21 resolution. In order to mitigate systematic climate drifts, a “Q-flux” adjustment was applied to the net surface flux (Hansen et al., 1997). Since the forcings imposed on the models (i.e., top-of-the-atmosphere insolation, Q-flux, land surface albedo) consisted of climatological mean values, the simulated SSTA variability reflects each model’s chaotic internal variability. In what follows, we use as our measure of persistence (denoted as τ_p) the time for which the value of the SSTA autocorrelation function drops to e^{-1} .

Overall, the τ_p as simulated by QTCM1 and CCM3 manifest some gross similarities to one another (Figure 1). In fact, the spatial pattern correlation coefficient of the two models is strongly statistically significant, i.e., $r = 0.51$ for the entire ocean or 0.56 for 30°S – 30°N . Extremely long persistence times, $\tau_p > 400$ days, extend along the near-equatorial Pacific from $\sim 150^\circ\text{W}$ eastward to the coastline of South America. Lengthy persistence is also evident in the southeast tropical Atlantic, and to a lesser extent the south Indian Ocean and high latitudes of both hemispheres. Short persistence times, on the order of 30–60 days, occur in the north Indian Ocean, the equatorial Atlantic and South Atlantic Tropical Convergence Zone, and in an arc-shaped region of the western Pacific comprising the South Pacific Convergence Zone and the western Pacific warm pool region.

We point out that the geographic distribution of tropical τ_p broadly resembles the distribution of mean convection, especially in QTCM1 (Figure 1, line contours). The regions of weakest mean oceanic convection—the eastern equatorial Pacific, the southeast Atlantic, and south Indian Ocean—are characterized by the most persistent mixed layer SSTAs. In later sections, we explore the origins of the long persistence/slow decay of nonconvecting region SSTAs using a simplified analytic framework.

At this point, we briefly comment on the relationship of the passively coupled simulations to the observed autocorrelation persistence in the Tropics. As shown in previous studies, the spatial structure of tropical τ_p is heavily affected by ENSO (c.f., Figure 2 of Wu and Newell, 1998): in particular, long persistence times, on the order of 200 or more days, are noted in the equatorial eastern Pacific source region of ENSO as well as those remote regions which are strongly teleconnected to ENSO (e.g., the north tropical Atlantic and the western Indian Ocean). We find it intriguing that the passively-coupled models examined here manifest such lengthy persistence in the ENSO source region, even though the ocean dynamics responsible for ENSO are absent. It seems plausible that the slow decay regime prevailing in the eastern Pacific in the passive coupling case may impact the active dynamics of ENSO, e.g., the frequency, duration, and magnitude of ENSO events, although this is beyond the scope of the present study.

Apart from the spatial structure of τ_p , it is also of interest to ask what happens to the decay characteristics as successively larger spatial scales are considered. Coupling between gridpoints, via the atmosphere, may substantially alter decay times, following the arguments in Section 1. To reiterate, as the spatial extent of SSTAs (or the spatial extent of anomaly correlations) increases, the persistence should increase (or the rate of decay should slow) as different regions compete and the efficiency of net energy export is reduced.

Indeed, simple spatial aggregation of SSTA hints at the lengthening of τ_p as larger areas are considered. For example, for QTCM1, the mean, gridpoint-averaged τ_p for the entire Tropics (30°S-30°N) is 125 days (or 106 days for mean convecting regions with precipitation exceeding 1 mm day⁻¹). On the other hand, the decay time for the Tropics, considered as a whole, is roughly 70 days longer. The decay time for the global-averaged ocean is nearly 315 days. Similar behavior is evident for CCM3, albeit with a much more pronounced increase of decay at larger scales.

3. Eigenvalue analysis

The interpretation of decay characteristics derived from autocorrelation persistence is subject to significant ambiguity. For one thing, the autocorrelation approach describes the temporal persistence of variability without regard to its spatial structure. However, the decay characteristics of an SSTA fluctuation in a given region may depend nontrivially on the behavior of remote SSTA fluctuations, e.g., a warm anomaly of given magnitude might be expected to decay more rapidly if it occurs in isolation than if it occurs as part of a broader pattern of warm anomalies. The autocorrelation may further reflect contributions from multiple decay timescales: for instance, the initial decay of an SSTA may be faster compared to subsequent periods as local or remote feedbacks arise in response to the anomaly. Clearly, an approach which can account for some of these complexities is desirable. Thus, in this section, we employ a simple eigenvalue analysis that provides some insight into the spatial structure of the SSTA decay as well as its modal nature.

a. Method

To implement the eigenvalue analysis, we estimated a linear, steady-state model of the atmospheric heat fluxes to surface temperature perturbations from ensembles of QTCM1 simulations. The oceanic domain was first divided into N basis regions. The model was then integrated N times, with the perturbation forcing consisting of a 1K increase in a specified basis region and no perturbations in all other regions. For each simulation, the net surface flux—the sum of surface radiative and turbulent fluxes—was obtained for all basis regions; surface flux anomalies (ΔF) were then defined as differences between each basis region simulation and a control run with zero-valued surface temperature perturbations everywhere. The procedure was repeated M times and ensemble averaged ΔF were obtained.

The time rate of change of the perturbation surface temperature field can be written as:

$$c_{M_i}^k \partial_t \Delta T_{sk} = -G_i^j \Delta T_{sj} \quad (5)$$

where $c_{M_i}^k$ is a diagonal matrix of basis region heat capacities and G_i^j is a sensitivity matrix relating i^{th} region ΔF to j^{th} basis region perturbation forcing. It is straightforward to solve equation (5) as a simple matrix eigenvalue problem; the general time-dependent solution for an arbitrary distribution of surface temperature perturbations $\mathbf{SST}(\mathbf{0})$ is (in matrix notation):

$$\Delta \mathbf{T}_s(\mathbf{t}) = \mathbf{V} \mathbf{D} \mathbf{V}^{-1} \mathbf{T}_s(\mathbf{0}) \quad (6)$$

where \mathbf{V} is the eigenvector matrix of $\mathbf{c}_M^{-1} \mathbf{G}$ and \mathbf{D} is a diagonal matrix with elements $e^{-\lambda_i t}$, with the λ_i 's representing the eigenvalues of $\mathbf{c}_M^{-1} \mathbf{G}$. For simplicity, we consider a spatially-invariant 50 m mixed-layer.

b. Eigenvalue analysis applied to basin scale SST forcing

Eigenvalue analysis was first applied to basis regions corresponding to the scale of ocean basins, with $N=5$ basis regions: the tropical Pacific (PAC), Atlantic (ATL), and Indian (IND) Ocean basins as well as the entire Northern and Southern Hemisphere extratropical oceans for latitudes poleward of 30° (NH EXT and SH EXT). Results of this eigenvalue analysis are summarized in Table 1.

The leading eigenmode (Mode 1) is characterized by a decay timescale of nearly 500 days. This decay time is roughly 40% greater than the largest local decay time, as estimated from the diagonal entries of \mathbf{G} , or $\sim 130\%$ larger than the area-weighted mean of basin scale local decay times (218 days). Clearly, Mode 1 reflects enhanced persistence (or slower decay) relative to the locally-estimated decay times. Examination of the sensitivity matrix suggests why this is the case: while the diagonal matrix elements are negative—corresponding to SSTA decay within the region in which the SST perturbation is imposed—the off-diagonal matrix elements are typically positive—i.e., the mixed layer tends to warm away from the location of the imposed SSTA. Flux cancellation between diagonal and off-diagonal elements results in at least one eigenmode with a decay timescale exceeding the local decay values.

Spatially, the leading mode exhibits the broadest, most uniform spatial structure, as evidenced by the large spatial mean and small spatial standard deviation of the leading eigenvector relative to the remaining ones. However, while the projection of the leading mode is of the same sign in all regions, the loading varies by a factor of ~ 4 across the 5 basis regions, with its strongest projection in the SH EXT region, where the local decay time is largest. The heterogeneity of the slowest decay mode reflects variations in basic state climatology, a point to which we return in Section 5. Apparently, the leading eigenmode convolves the broad scales anticipated for the most slowly-decaying mode with localized regions of slow decay.

The remaining eigenmodes exhibit decay times that are more-or-less comparable to the local decay times. For instance, the decay time of the 2nd mode lies between the decay time of SH EXT and the remaining regions. The Mode 2 eigenvector is of one sign in SH EXT and of the opposite sign elsewhere. Mode 3 behaves similarly, but with its projection of one sign in PAC and opposite sign elsewhere. The loadings of Modes 2 and 3 suggest isolation of the slowest decay regions, although their separation is not clean. Also, the occurrence of complex solutions (as in modes 4 and 5, which are complex conjugates) points to oscillatory behavior rather than strict exponential decay.

c. Eigenvalue analysis applied to subbasin scales

To elucidate smaller scale spatial structures, the three principal tropical ocean basins were subdivided into smaller regions; the shapes and numbers of basis regions used for each basin ($N = 19$ for the Pacific; $N = 8$ for the Atlantic; $N = 6$ for the Indian) were chosen to give comparable numbers of gridpoints within each ocean surface patch. However, before considering the results of the subbasin eigenvalue analysis, it is first necessary to address the nonlinearities in the net surface flux response.

An underlying assumption of the eigenvalue approach is that the flux response to an imposed distribution of SSTA forcing is linear: i.e., the flux response to a set of basis regions, summed

over the entire domain, should be identical to the net flux response to a different basis set with the same total forcing applied to all regions. However, for $N = 35$ regions, significant departures from linearity are found to occur. The difference between the net surface flux responses for the subbasin and basin scale analyses points to nonlinear effects, most likely associated with the interaction between the SSTA forcing and QTCM1's mid-latitude wave dynamics: large differences in net surface flux amplitudes were noted in the vicinity of the Northern Hemisphere mid-latitude winter storm tracks. Possible sources of the nonlinearity include anomalous advection of heat and moisture associated with the model's baroclinic wave dynamics, windspeed dependences in surface flux parameterizations, and nonlinearities in QTCM1's convective parameterization.

To mitigate the nonlinearity arising in the transition to smaller scales, we applied eigenvalue analysis to a set of simulations in which temperature and moisture advection were artificially modified. In particular, these quantities were replaced by their mean values (including mean transient advection) plus contributions from anomalous temperature and moisture gradients advected by mean winds. Contributions to temperature/moisture advection from mean gradients advected by anomalous winds as well as anomalous gradient advection by anomalous winds were suppressed.

The spectrum of the real part of modal decay times for the modified simulations, sorted from slowest to fastest, is illustrated in Figure 2, with local decay time estimates displayed for comparison. The leading mode, with $\tau_{decay} = 563$ days, lies well above any of the local decay estimates. (It should be noted that the decay timescale of the leading mode is approximately 10% longer than the slowest decay mode of the $N = 5$ case. The lengthening of the leading decay time is likely a consequence of the alteration to the model's advection scheme.) In contrast to the leading eigenmode, nonleading modal decay times fall below at least one of the local decay time estimates.

Eigenvector loadings of the first three modes are displayed in Figure 3. Like the leading eigenmode of Section 3b, the leading mode of the $N = 35$ case (Figure 3a) exhibits the lowest spatial standard deviation to spatial mean ratio, consistent with expectations of a broad structure for the slowest decay mode. While the first eigenvector loading is of the same sign everywhere,

the amplitude of the eigenvector loading is quite variable regionally, with the strongest loading in the SH extratropics. The structure of the leading eigenmode loading again underscores relatively unclear separation between the slowly-decaying, spatially-broad mode and localized regions of slow decay.

The second leading mode (Figure 3b) is characterized by both positive and negative loadings. Especially notable is the sign difference between the extratropical Northern and Southern Oceans. Those regions of the Tropics with the slowest decay seen in Section 2, the southeast tropical Pacific and Atlantic Oceans, are also emphasized. The third mode is positive in most of the tropics (negative in the northern and southern extratropics) and the region of slow local decay in the eastern Pacific is highly weighted.

When the extratropical oceans are excluded from the eigenanalysis, the separation in modal loading of the eastern Pacific and southeast Atlantic Oceans from the rest of the Tropics is again a dominant spatial feature of the leading eigenmodes. Figure 3d shows the leading mode of the Tropics-only case. It has a broad positive structure but with particularly high loading in the southeastern Pacific and negative loading in the southeastern Atlantic. These spatial features are similar to mode 3 of the global case, although the Tropics-only mode reflects a longer decay time (329 days versus 237 days), since canceling fluxes in the extratropics are absent.

Since QTCM1 is not optimized for extratropical accuracy, and we have used much broader extratropical basis regions, the global case is shown primarily to provide a sense of how the Tropics-only computation is modified by inclusion of the extratropics. Physically, the Tropics-only configuration is likely of more relevance to forcing spread by equatorial wave dynamics, while modes 1 and 2 of the global computation would require truly global or hemispheric scale forcing to be excited. In the remainder of the paper we thus address issues of how the inhomogeneity in the basic state influences decay time scales and spatial patterns in the Tropics-only case.

4. Analytic prototype for SST decay spatial scale dependence

Following the approach of SN05, we consider a set of (perturbation) equations for T_s and T as well as specific humidity (q) for the tropical climate system:

$$c_M \partial_t T_s = \epsilon_{T_s}^{T_s} T_s + \epsilon_T^{T_s} T + \epsilon_q^{T_s} q \quad (7)$$

$$c_A \partial_t T = \epsilon_{T_s}^T T_s + \epsilon_T^T T + \epsilon_q^T q - M_s \nabla \cdot \bar{\mathbf{v}} - \overline{M_s} \nabla \cdot \mathbf{v} \quad (8)$$

$$c_A \partial_t q = \epsilon_{T_s}^q T_s + \epsilon_T^q T + \epsilon_q^q q + M_q \nabla \cdot \bar{\mathbf{v}} + \overline{M_q} \nabla \cdot \mathbf{v} \quad (9)$$

Here, the coefficients ϵ_j^k are flux sensitivity coefficients (in units of $\text{Wm}^{-2}\text{K}^{-1}$; see Appendix A for definitions); M_s and M_q are dry static stability and moisture stratifications, respectively; and $\nabla \cdot \mathbf{v}$ is the divergence. Overbars denote prescribed mean state values; all other values are assumed to be perturbations with respect to the mean state. The moisture is in Kelvin, absorbing L/c_A in q , and the time derivatives of T and q , shown here for completeness, are neglected in the analysis, since they are associated with fast atmospheric time scales.

T_s , T , and q are regarded as functions of a generalized horizontal spatial coordinate, x . For simplicity, a homogeneous, convecting mean-state (for which $\nabla \cdot \bar{\mathbf{v}} = 0$) is considered. The flux sensitivity coefficients are assumed spatially invariant, including the windspeed dependences in turbulent fluxes, and horizontal advection is ignored. Cloudiness impacts on shortwave and longwave radiative fluxes are not included. Also, the strict QE-limit (Neelin and Zeng, 2000) of vanishingly small convective adjustment timescale is invoked. Since strict QE implies $q \approx nT$, equations (8)-(9) can be replaced by a single moist static energy equation in T only.

In addition to equations (7)-(9), we consider a diagnostic momentum equation of the form:

$$r \partial_x T = \epsilon_u^u u \quad (10)$$

i.e., the baroclinic temperature (or pressure) gradient balances (surface) friction. Assuming separable form solutions, i.e., $T_s(x, t) = \sum \sum \tilde{T}_s e^{ikx/Re} e^{\lambda t}$, we obtain a dispersion relationship of the

form:

$$\lambda = c_M^{-1} \left[\epsilon_{T_s}^{T_s} - \frac{(\epsilon_{T_s}^{T_s} + n\epsilon_q^{T_s})(\epsilon_{T_s}^T + \epsilon_{T_s}^q)}{[\epsilon_{T_s}^T + n(\epsilon_q^T + \epsilon_q^q)](1 + k^2/k_0^2)} \right] \quad (11)$$

where R_e is the radius of the earth, $k_0^{-1} = R_e \sqrt{\frac{rM}{\epsilon_{T_s}^* \epsilon_u^u}}$, and $L_0 = R_e k_0$ defines a damping length scale over which tropospheric temperature anomalies behave coherently.

Decay spectra for $k_0 = 0, 1, 2,$ and 3 appear in Figure 4. In the inviscid limit $\epsilon_u^u \rightarrow 0$, the scale defined by L_0 becomes infinite, i.e., temperature fluctuations behave coherently throughout the entire domain. In this weak temperature gradient (WTG) regime, the decay at all nonzero wavenumbers is fast compared to the decay at wavenumber 0. For nonzero k_0 , there is a smooth transition between the slowest-decay mode at $k = 0$ and the faster, effectively local decay values determined by $\epsilon_{T_s}^{T_s}$ for $k > k_0$. For parameter values representative of the Tropics, $k_0 \approx 1.5$. Thus, we expect only a small number of modes should exhibit decay timescales differing significantly from local decay values, in agreement with what is seen in Figure 2.

The diagnostic balance between baroclinic gradients and frictional damping admits real (and decaying) solutions for λ . However, other balances are plausible, e.g., baroclinic pressure gradients and momentum advection. In general, this balance yields complex solutions for λ , i.e., solutions that propagate as well as decay. Such solutions may well be relevant to the timing of interbasin adjustment processes, but these are beyond the scope of the current study.

5. Analytic prototype for differences between convecting and nonconvecting regimes

The prototype developed below offers insight into the separation between the fast local decay times of tropical convecting regions and the slow local decay of nonconvecting regions. However, as we demonstrate, the prototype sheds light on the interpretation of the eigenvalue analysis (Section 3), specifically for understanding the blending that occurs between the broad-scale, slow decay modes and the slow, local decay times characteristic of tropical nonconvecting regimes.

a. The N -box WTG model

Consider discretization of equations (7)-(9) (again assuming WTG) over a domain consisting of N boxes. Numerical solution of these equations under perturbation surface temperature forcings analogous to the eigenvalue analysis of Section 3 (i.e., imposing unit SSTAs separately in each of the boxes) yields an $N \times N$ atmosphere heat flux matrix, from which eigenvalues are computed. We are interested in what happens when convection is varied within a subset M of the boxes, with a parameter α_c denoting the convective fraction within the subset. (One interpretation for α_c is that it represents the time the subset M spends convecting; alternatively, it can represent the spatial fraction of M experiencing deep convection.) The limit $\alpha_c = 0$ corresponds to the totally nonconvecting limit, while $\alpha_c = 1$ the fully convecting limit. (In the latter case, all N boxes are identically convecting.) Eigenvalues of these simulations, as a function of α_c , are illustrated in Figure 5a for $N = 4$ and $N = 8$ total boxes, and $M = 1$ and $M = 2$, respectively. Here, we refer to the subset M as the “partially convecting region.”

Consider the fully convecting limit $\alpha_c = 1$, which corresponds to the left-most points in Figure 5a. For both $N = 4$ and $N = 8$, there are two eigenvalues. The mode with the smaller eigenvalue (or slower decay time) projects uniformly across each region; we refer to this slow decay mode as the “global” or “G” mode. The remaining modes, the “local convecting” or “LC” modes, are $(N - 1)$ -fold degenerate and decay significantly faster than the G mode. The eigenvectors of the LC modes are approximately sinusoidal, although the finite size of the boxes modifies their spatial characteristics.

As α_c is decreased, distinct eigenvalues emerge for the partially convecting region. For $N = 4$, a single mode with a decay timescale intermediate between the LC and G modes emerges; for $N = 8$, there are two such modes (since $M = 2$). In what follows, we refer to these modes as the “partially convecting” or “PC” modes in this section. In the limit of $\alpha_c = 0$ we also use the term “nonconvecting” or “NC” modes. The PC eigenvector loadings are largely confined to the

partially convecting region, and the eigenvalues (which are not strictly degenerate for $M > 1$) remain close to one another even as the decay times vary significantly over the range of α_c . The similarity of PC modal decay rates for small α_c hints that the partially convecting region decay times are relatively insensitive to the size of the SSTA within the partially convecting region, a point to which we return below.

The LC eigenvalue changes little with α_c . The G mode eigenvalue varies only slightly with α_c , in part because the partially convecting region is a relatively small portion of the total domain as well as for reasons elaborated below. When α_c is small, the PC decay times become comparable to the G mode decay time. As a result, the eigenvectors of the G and PC modes are altered in such a way that they become less distinct, i.e., the spatial characteristics of these modes are mixed. In general, as α_c decreases, the loading of the G mode eigenvector in the reduced convection region is diminished, and may even change sign. The PC mode, on the other hand, tends to have opposite loadings in the partially and fully convecting regions, with the loading in the latter region decreasing as α_c decreases.

b. A 2-box model for the global and reduced convection modes

The case for which the PC and G decay times are much slower than the LC decay timescales is relevant to the passively-coupled tropical ocean-atmosphere system. We exploit the separation of LC eigenvalues to replace the arbitrary N-box model by a simple $N = 2$ system. Box 1, with an area size fraction f_1 , is fully convecting, while box 2, with an area size fraction $f_2 = 1 - f_1$, has specified convective fraction α_c as in the N-box case. As with the prototype of Section 4, the strict QE limit and constant gross moist stability M are assumed in box 1 and the convecting fraction of box 2. SSTAs imposed in box 2 are assumed not to alter α_c .

Although this model can be treated as a literal 2-box model, its true utility lies in its capacity to approximate the N -box model closely in certain parameter ranges, eliminating redundant degenerate solutions. Furthermore, its straightforward analytic solution elucidates the behavior of

the G and PC modes. Specifically,

1. The 2-box solutions approximate the G and PC modes over a large range of parameters (i.e., f_1 greater than roughly 0.3, and small to modest α_c). In the N-box case, the set of convecting region boxes is characterized by identical eigenvector loadings for the G and PC modes and may thus be replaced by box 1 in the 2-box model. This gives an excellent approximation to these two modes, as seen in Figure 5b. The case $f_1 = 0.75$ may be compared to the numerical case in Figure 5a, with the caveat that the differences seen are the result of using a finite convective time scale in the latter. (Note that the degenerate LC modes in Figure 5b are obtained in a separate calculation; see #3.)
2. Analysis of the PC region time scale in the nonconvecting ($\alpha_c = 0$) limit provides insight into why the reduced convection region exhibits slow decay.
3. Other limits of the 2-box model are useful for other purposes, e.g., for f_1 small and $\alpha_c=1$, the 2-box model yields G and LC modes.

Analytic expressions for the steady state T , q , and $\nabla \cdot \mathbf{v}$ in the 2-box framework are outlined in Appendix B. Here we note that the 2×2 surface flux sensitivity matrix to unit SSTAs is:

$$\mathbf{G} = \begin{pmatrix} \epsilon_{T_s}^{T_s} + (\epsilon_T^{T_s} + n\epsilon_q^{T_s})T(1, 0) & \epsilon_T^{T_s}T(1, 0) + \epsilon_q^{T_s}q_2(1, 0) \\ (\epsilon_T^{T_s} + n\epsilon_q^{T_s})T(0, 1) & \epsilon_{T_s}^{T_s} + \epsilon_T^{T_s}T(0, 1) + \epsilon_q^{T_s}q_2(0, 1) \end{pmatrix} \quad (12)$$

where $T(1, 0)$ and $T(0, 1)$ are tropospheric temperature perturbation associated with unit SST perturbations in boxes 1 and 2, respectively, and $q_2(1, 0)$ and $q_2(0, 1)$ are box 2 moisture values for the same cases. The eigenvalues of (12) are simply $\lambda_{\pm} = \frac{1}{2}(G_{11} + G_{22}) \pm \frac{1}{2}D^{1/2}$ where the discriminant D is given by $D = (G_{11} - G_{22})^2 + 4G_{12}G_{21}$.

Some insight into the behavior of the eigenvalues can be obtained by examining the behavior of the diagonal and off-diagonal matrix elements of \mathbf{G} (Figure 6). Consider parameters values

for which the squared difference between diagonal elements (Figure 6a) is large compared to the product of the off-diagonal terms. Then, the eigenvalues are approximately given by G_{11} and G_{22} . The behavior of G_{11} is easily understood. In the limit of vanishing f_1 , $T(1, 0)$ is identically zero, so $G_{11} = \epsilon_{T_s}^{T_s}$. As α_c increases, $T(1, 0)$ increases (linearly), and since $\epsilon_T^{T_s}$ and $\epsilon_q^{T_s}$ are of opposite sign to $\epsilon_{T_s}^{T_s}$, the magnitude of G_{11} decreases. Thus, the two limits $f_1 = 0$ and $f_1 = 1$ correspond to the fast LC and slow G modal decay times, respectively.

As suggested by Figure 6b, the off-diagonal terms G_{21} and G_{12} are generally small for the parameter values assumed here, especially G_{21} , which gives the effect of partially convecting region SSTA on the fully convecting region. The smallness of these terms explains why the eigenvector loadings of the G and PC modes are small in the reduced and fully convecting regions, respectively. Further, as Figure 6a indicates, the diagonal terms G_{11} and G_{22} may approach one another; in this case, the off-diagonal terms may significantly modify the eigenvalues.

For the parameter values assumed, G_{12} and G_{21} are positive, so both terms in the discriminant D are positive. However, under certain circumstances, the effect on the PC region of (say) an anomalous warm SST in the fully convecting regions can cause G_{21} to change sign. This occurs because: (1) on the one hand, tropospheric temperature increases over the partially convecting region, leading to enhanced longwave warming of SST; (2) while on the other hand, descent anomalies suppress moisture, thereby increasing evaporation which has a cooling tendency. The competition between warming and drying determines the sign of G_{21} .

For the nonconvecting limit, the main case of interest, the matrix elements in Figure 6 are relatively insensitive to f_1 when it exceeds 0.3. Thus, the behavior of a small nonconvecting region is therefore a good prototype for that of one that represents even a modest fraction of the total tropical domain.

c. Why nonconvecting regions exhibit slow decay

The assumption of strict QE means that T and q vary in concert, but even for finite convective adjustment timescales, convecting region temperature and humidity anomalies must vary closely on timescales relevant to SST decay. The behavior of G_{22} is distinct from G_{11} since T and q perturbations in box 2 become less tightly coupled as α_c decreases. Take the case of $\alpha_c = 0$ with an SST perturbation imposed in box 2. The box 2 moisture equation in the nonconvecting limit is just $\overline{M}_q^{nc} \nabla \cdot \mathbf{v}_2 + M_{qp} \nabla \cdot \overline{\mathbf{v}}^{nc} q_2 + E = 0$. When the nonconvecting region is relatively small, $f_2 \rightarrow 0$, $T(0, 1) = 0$,

$$\nabla \cdot \mathbf{v}_2 = \overline{M}_s (\epsilon_{T_s}^T T_{s2} + \epsilon_q^T q_2), \quad (13)$$

so

$$q_2 = \frac{\gamma \epsilon_H + \overline{M}_q \overline{M}_s^{-1} \epsilon_{T_s}^T}{b \epsilon_H - M_{qp} \nabla \cdot \overline{\mathbf{v}}^{nc} - \overline{M}_q \overline{M}_s^{-1} \epsilon_q^T} T_{s2} \quad (14)$$

Even though there is no temperature perturbation, $q_2(0, 1)$ is nonzero and positive (since both numerator and denominator are both positive) since it rises with evaporation until balance is achieved.

For the parameter values given in Table 2, the first terms in both the numerator and denominator of (14) are roughly 2-3 times as large as the remaining terms. Expanding the denominator to first order in the terms small compared to $b \epsilon_H$, q_2 becomes:

$$q_2 \approx (\gamma/b) [1 + (M_{qp} \nabla \cdot \overline{\mathbf{v}}^{nc}) / (b \epsilon_H) + (M_q \epsilon_{T_s}^T / M_s) / (\gamma \epsilon_H) + (M_q \epsilon_q^T / M_s) / (b \epsilon_H)] \quad (15)$$

The latent heating, sensible heating, and net surface radiative components of the total surface heat flux for the nonconvecting region (i.e., G_{22}) are then:

$$E \approx -[(\gamma M_{qp}/b) \nabla \cdot \overline{\mathbf{v}}^{nc} + (M_q/M_s)(\epsilon_{T_s}^{surf} - \epsilon_{T_s}^{toa} + \epsilon_H) + (\gamma/b)(M_q/M_s)(\epsilon_q^{surf} - \epsilon_q^{toa})] T_{s2} \quad (16)$$

$$H = \epsilon_H T_{s2} \quad (17)$$

$$R_s \approx [\epsilon_{T_s}^{surf} + \epsilon_q^{surf}(\gamma/b)]T_{s2} \quad (18)$$

The evaporation comprises contributions from (slow) mean subsidence [the first term on the RHS of (16)] as well as feedback terms associated with changes to the circulation. The contribution of the mean subsidence term, which tends to be the largest single component of the net surface flux, implies $E \propto$ moisture divergence, which significantly limits the evaporation rate.

The remaining terms are associated with atmospheric absorption of anomalous fluxes from the surface, which lead to anomalous ascent opposing the climatological descent. The resulting decrease in evaporation tends to partially compensate for the upward surface fluxes, e.g., longwave radiation and sensible heat flux, equations (17) and (18), that act to cool SST. As an example, consider the effect of the term associated with upward longwave radiative cooling of the surface associated with the direct effect of anomalously warm SSTA [the first term on the RHS of (18)]. Writing the portion of emitted longwave absorbed by the atmosphere as $\delta = (\epsilon_{T_s}^s - \epsilon_{T_s}^t)/\epsilon_{T_s}^s$, the net cooling when including the feedback effect in evaporation reduces the direct longwave cooling by a factor of approximately $(1 - \overline{M}_q \overline{M}_s^{-1} \delta)$. Since M_q is a large fraction of M_s and a large fraction of long wave is absorbed, this amounts to a substantial reduction. Similar arguments apply to the longwave flux associated with changes to moisture as well as the sensible heating.

Thus for a small nonconvecting region, the rate of evaporative cooling is limited by the slow moisture divergence, and other forms of surface cooling absorbed in the troposphere are reduced by feedbacks via the circulation onto evaporation. This results in a much slower decay than for a small convecting region. An alternative explanation for the slowness of nonconvecting region decay was put forth by Chiang and Sobel (2002). Specifically, in the absence of deep convection, the communication between the free tropospheric temperature and the surface is limited, since the timescale for vertical advective transport is much slower than the timescale for vertical convective transport. Because q and T are effectively decoupled within nonconvecting regions, the former can buffer surface temperature from the free tropospheric temperature, which limits the capacity for the SSTA to decay.

The behavior of G_{22} further suggests that the nonconvecting region decay time should change little as the size of the nonconvecting region is varied (for a region with small α_c). This is because there is no convective feedback on the warming by surface fluxes, so T remains small, and the balances remain similar to the case just discussed.

d. Merger of the G and NC modes

Previously, we noted the role of horizontal transports in setting decay timescales, particularly for the most slowly-decaying modes. For the calculations in Figure 5, the damping coefficients ϵ_T^{tr} and ϵ_q^{tr} , representing transport to the extratropics, are set to zero, which results in rather long (>1000 day) decay times for the G mode.

However, small changes to these damping coefficients can have a strong impact on the eigenvalues: in Figure 7a, the two damping coefficients (assumed equal for simplicity) were varied over a realistic range of values for $f_1 = 0.6$ for $\alpha_c = 0$. By increasing (say) the temperature damping, the tropospheric temperature warming is lowered relative to the no-damping situation; this results in a decrease to G_{11} . (G_{22} also decreases, but the change is less pronounced.) Thus, the nonconvecting region mode and global decay modes eigenvalues increase—and in fact converge—as the damping increases.

For zero damping and $f_1 = 0.6$, G_{12} and G_{21} are both small, so the off-diagonal terms have little impact on the eigenvalues. However, the convergence of diagonal matrix elements as damping increases means that the off-diagonal terms may become more significant. In fact, as the damping increases beyond $\epsilon_T^{tr} \approx 0.3$, the sign of G_{21} changes for the reason discussed in Section 5b. The discriminant changes sign when $(G_{11} - G_{22})^2$ becomes less than $4G_{12}G_{21}$. Thus, a complex conjugate pair replaces the two real eigenvalues for damping values greater than $\epsilon_T^{tr} \approx 1.85$.

This case provides a simple illustration of the blending of properties that may occur between eigenmodes. This can occur even if the eigenvalues do not become equal, as in the case shown, but simply become sufficiently close. In particular, the properties of the global mode—which for

physically-realistic climatologies is the most slowly-decaying mode characterized by the broadest spatial scale—become mixed with the properties of slowly-decaying reduced convection region modes. This behavior is what produces the spatial inhomogeneity seen in the eigenvalue analysis of the full QTCM1 simulations (Section 3). The regions of slowest local decay appear with high loadings in the slow global mode of the tropical case because of this blending effect, since the time scales are not well separated. The slow nonconvecting regions can appear with either sign within the global mode for either of two reasons. One is if the affect of convecting region SSTA actually creates a cooling in the nonconvecting region, as noted above. The other, as seen for instance in Figure 3, is simply that if there is more than one slow decay region, they will tend to occur with opposite sign in the leading eigenmodes.

6. Summary and conclusions

The spatial inhomogeneity of autocorrelation times in atmospheric models (CCM3 and QTCM1), when coupled to an ocean mixed layer, motivates a systematic study of the modes of the passively coupled system. When inhomogeneity is ignored, the physics underlying the local and global decay timescales is straightforward. For small-scale SST anomalies, decay times are typically rapid: for a 50 m mixed layer, e-folding times of order 50-100 days are obtained. Because the atmospheric response to a localized heating anomaly is spread by transport over large distances, mixed layer heat content is rapidly extracted from sufficiently localized anomalies. As the size of the SSTA increases, the decay rate becomes progressively limited by relatively slow top-of-the-atmosphere radiative transfer. Consequently, for a global SST anomaly, for which the size of the SST anomaly is comparable to the total radiating area of the atmosphere, the decay time exceeds 500 days for a 50 m mixed-layer depth.

Under more realistic conditions, the transition between the two scales is nontrivial, because of differences between tropical and extratropical dynamics and basic state inhomogeneities. Within the tropics, efficient horizontal wave dynamics communicates the heating from local sources over

the extent of the equatorial waveguide, $\sim 20^{\circ}\text{S}$ - 20°N . Eigenvalue analysis of idealized simulations indicates that local decay is a reasonable approximation for scales smaller than roughly that of tropical Atlantic or Indian basins. Extratropical wave dynamics also affects SST decay characteristics, although in a more complicated way, e.g., nonlinearities associated with midlatitude wave dynamics impart a nontrivial structure to the decay characteristics.

A major focus of this study concerned the impact of basic state climate on tropical decay characteristics. In particular, we noted the distinct separation of local tropical SST decay timescales for mean convecting and nonconvecting regions, with the latter exhibiting decay timescales several times longer than the former. The reason for this was underscored in Section 5: for nonconvecting regions, the dominant balance is between slow moisture divergence via the subsiding mean flow and evaporation. In the absence of a convective moisture sink, sizable tropospheric humidity anomalies develop in response to SSTAs imposed within the nonconvecting region. These anomalies limit the rate of evaporation to a value given by the slow moisture divergence, in turn implying a slow rate of SST decay. Longwave surface cooling is substantially absorbed in the atmosphere, which slows moisture divergence, and thus likewise has a limited effect in causing SST decay.

The slow decay of nonconvecting regions has significant ramifications for the structure of passive ocean-atmosphere decay modes, especially the slowly-decaying global mode. While the global decay mode might be expected to exhibit a broad, uniform spatial structure, this does not hold in the presence of basic state inhomogeneities: although eigenvalue analysis indicates a relatively broad structure for the most slowly decaying mode, its structure is far from uniform. In particular, the features of the global decay mode are blended or mixed with the localized, slow decay characteristics of nonconvecting areas. Precisely how this blending affects the eigenmodes depends quite strongly on the closeness of the time scales and other parameters: the loading of nonconvecting region in the global mode can have relatively small or large amplitude or even change sign. If the nonconvecting and global mode time scales approach each other, merger may even occur. In an eigenvalue analysis based on a flux sensitivity matrix from QTCM ensemble

runs, the most visible signature is large eigenvector loadings of the slow, leading eigenmodes in localized slowly decaying regions.

Although we have phrased results largely in terms of the decay of SSTAs, the results also apply to passive mixed layer equilibration to a prescribed climate forcing, e.g., the remote tropical climate response to El Niño or the transient upper ocean adjustment to atmospheric radiative anomalies associated with greenhouse gases or aerosols. For instance, SN05 argued that tropical tropospheric warming to El Niño can be viewed in two stages: a fast stage, associated with energy loss to the unadjusted remote mixed layer, and a slower stage—essentially the global tropical decay timescale—limited by top-of-the-atmosphere radiative losses and tropical-extratropical energy export.

The results of our study add a further layer to this picture of the tropospheric temperature adjustment to El Niño, specifically with respect to the impacts of basic state inhomogeneities. Consider, for example, the tropical Atlantic. Because of the Northern Hemisphere bias of the Intertropical Convergence Zone, the north tropical Atlantic is, on average, more strongly convecting than the south tropical Atlantic. Thus, we anticipate modifications to the rate of tropospheric warming from the local convective and nonconvective region decay modes operating to the north and south of the equator, respectively. We thus conjecture that the inhomogeneous passive decay modes examined here may be useful ingredients in understanding the observed tendency for an equatorially-asymmetric tropical Atlantic surface temperature response to El Niño, with regions north of the equator warming more, and with different timing, than those to the south (Enfield and Mayer 1997; Elliot, 2001; Chiang and Sobel, 2002). Equally intriguing, and warranting further study, is how the slow decay region in the nonconvecting southeastern Pacific, encountered here with only passive coupling, interacts with ocean dynamics in the ENSO source region of the equatorial Pacific.

Acknowledgments. We thank John Chiang for use of the CCM3 mixed layer simulation. We also thank Tom Farrar for valuable discussion and comments on the manuscript. This work was supported in part by NOAA grants NA04OAR4310013 and NA05OAR4311134 and NSF grant ATM-0082529. BRL further acknowledges partial support by John Chiang and NOAA grant NA03OAR4310066.

7. Appendix A: Flux sensitivity coefficients

The flux sensitivity coefficients are defined analogously to SN05. The values assumed are representative of clear-sky conditions. These coefficients are:

$$\epsilon_{T_s}^T = \epsilon_{T_s}^{surf} + \gamma\epsilon_H + \epsilon_H \quad (19)$$

$$\epsilon_q^T = b\epsilon_H + \epsilon_q^{surf} \quad (20)$$

$$\epsilon_T^T = a\epsilon_H + \epsilon_T^{surf} \quad (21)$$

$$\epsilon_{T_s}^T = \epsilon_H + \epsilon_{T_{surf}}^s - \epsilon_{T_s}^{toa} \quad (22)$$

$$\epsilon_{T_s}^q = \gamma\epsilon_H \quad (23)$$

$$\epsilon_T^T = \epsilon_T^{surf} - \epsilon_T^{toa} - a\epsilon_H - \epsilon_T^{tr} \quad (24)$$

$$\epsilon_q^T = \epsilon_q^{surf} - \epsilon_q^{toa} \quad (25)$$

$$\epsilon_T^q = 0 \quad (26)$$

$$\epsilon_q^q = -b\epsilon_H - \epsilon_q^{tr} \quad (27)$$

In the above expressions, a and b relate the QTCM1 vertical structure functions of temperature and moisture to their surface values, respectively. The coefficient γ , defined as $\frac{\partial q_s}{\partial T_s}$, where q_s saturation specific humidity at the surface, follows from the linearization of evaporation; it is evaluated with respect to a reference temperature, taken here to be 302 K. Values of the flux sensitivity parameters are summarized in Table 2. The temperature and moisture transport coefficients, ϵ_T^{tr} and ϵ_q^{tr} , are treated as adjustable parameters.

8. Appendix B: Analytic solutions to the 2-box model

Using the labeling conventions of Section 6, the temperature perturbation to an arbitrary distribution of SSTs T_{s1} and T_{s2} is:

$$T(T_{s1}, T_{s2}) = T^* [\overline{M}^{c-1} (f_1 + f_2 \alpha_c) (\epsilon_T^T + n(\epsilon_q^T + \epsilon_q^q)) + (1 - \alpha_c) f_2 \epsilon_T^T C_1]^{-1} \quad (28)$$

where $T^* = -[\overline{M}^{c-1} (\epsilon_{T_s}^T + \epsilon_{T_s}^q) (f_1 T_{s1} + f_1 \alpha_c T_{s2}) + (1 - \alpha_c) f_2 C_1 C_2 T_{s2}]$ and $C_1 = [\overline{M}_s^{nc} + \frac{\epsilon_q^T \overline{M}_q^{nc}}{M_{qp} \nabla \cdot \overline{\mathbf{v}}^{nc} + \epsilon_q^q}]^{-1}$ and $C_2 = \epsilon_{T_s}^T - \frac{\epsilon_q^T \epsilon_{T_s}^q}{M_{qp} \nabla \cdot \overline{\mathbf{v}}^{nc} + \epsilon_q^q}$.

For box 1, the humidity perturbation is, by the strict QE assumption, just $q_1(T_{s1}, T_{s2}) = nT(T_{s1}, T_{s2})$. For box 2, on the other hand,

$$q_2(T_{s1}, T_{s2}) = \alpha_c nT - (1 - \alpha_c) (\epsilon_{T_s}^q T_{s2} + \overline{M}_q^{nc} \nabla \cdot \overline{\mathbf{v}}_2) [M_{qp} \nabla \cdot \overline{\mathbf{v}}^{nc} + \epsilon_q^q]^{-1} \quad (29)$$

where $\nabla \cdot \overline{\mathbf{v}}_2(T_{s1}, T_{s2}) = C_1 (C_2 T_{s2} + \epsilon_T^T T(f_1, \alpha_c))$. Plots of the temperature and humidity anomalies in response to separate 1K SST perturbations in each box are illustrated in Figure 8.

REFERENCES

- Alexander, M.A., M. Newman, J.R. Lanzante, N.-C. Lua, and J.D. Scott, 2001: The atmospheric bridge: the influence of ENSO teleconnections on air-sea interaction over the global oceans. *J. Climate*, **15**, 2205–2231.
- Barsugli, J.J., and D.S. Battisti, 1997: The basic effects of atmosphere-ocean thermal coupling on midlatitude variability. *J. Atmos. Sci.*, **55**, 477–493.
- Battisti, D.S., 1988: Dynamics and thermodynamics of a warming event in a coupled tropical atmosphere ocean model. *J. Atmos. Sci.*, **45** (20), 2889–2919.
- Bhatt, U.S., M.A. Alexander, D.S. Battisti, D.D. Houghton, and L.M. Keller, 1998: Atmosphere-ocean interaction in the North Atlantic: Near-surface climate variability. *J. Climate*, **11**, 1615–1632.
- Bretherton, F.P., 1982: Ocean climate modeling. *Prog. Ocean.*, **11**, 93–129.
- Cane, M.A., and S.E. Zebiak, 1986: On the mechanism of the El Niño-Southern Oscillation cycle. In *Study Week on Persistent Meteo-Oceanographic Anomalies and Teleconnections*, edited by C. Chagas and G. Puppi, 6–96.
- Chang, P., 1998: Prediction of tropical Atlantic sea surface temperature. *Geophys. Res. Lett.*, **25**, 1193–1196.
- Chiang, J.C.H., and B.R. Lintner, 2005: Mechanisms of remote surface warming during El Niño. *J. Climate*, **18**, 4130–4149, doi:10.1175/JCLI3529.1.
- Chiang, J.C.H., and A.H. Sobel, 2002: Tropical tropospheric temperature variations caused by ENSO and their influence on the remote tropical climate. *J. Climate*, **15**, 2616–2631.
- Deser, C., M.A. Alexander, and M.S. Timlin, 2003: Understanding the persistence of sea surface temperature anomalies in midlatitudes. *J. Climate*, **16**, 57–72.
- Elliot, J.R., S.P. Jewson, and R.T. Sutton, 2001: The impact of the 1997/98 El Niño event on the Atlantic Ocean. *J. Climate*, **14**, 1069–1077.
- Enfield, D.B., and D.A. Mayer, 1997: Tropical Atlantic sea surface temperature variability and its

- relation to El Niño-Southern Oscillation. *J. Geophys. Res.*, **102**, 929–945.
- Frankignoul, C., and K. Hasselmann, 1977: Stochastic climate models 2: Application to sea-surface temperature anomalies and thermocline variability. *Tellus*, **29**, 289–305.
- Frankignoul, C., 1985: Sea-surface temperature anomalies, planetary-waves, and air-sea feedback in the middle latitudes. *Rev. Geophys.*, **23**, 357–390.
- Frankignoul, C. and E. Kestenare, 2002: The surface heat flux feedback. Part I: Estimates from observations in the Atlantic and North Pacific. *Clim. Dyn.*, **19**, 633–647.
- Gallego, B., and P. Cessi, 2001: Decadal variability of two oceans and an atmosphere. *J. Climate*, **14**, 2815–2832
- Giannini, A., J.C.H. Chiang, M.A. Cane, Y. Kushnir, and R. Seager, 2001: The ENSO teleconnection to the Tropical Atlantic Ocean: contribution of the remote and local SSTs to rainfall variability in the Tropical Americas. *J. Climate*, **14**, 4530–4544.
- Grabowski, W.W., 2006: Impact of explicit atmosphere-ocean coupling on MJO-like coherent structures in idealized aquaplanet simulations. *J. Climate*, **63** 2289–2306.
- Hansen, J., M. Sato, R. Ruedy, A. Lacis, K. Asamoah, K. Beckford, S. Borenstein, E. Brown, B. Cairns, B. Carlson, B. Curran, S. de Castro, L. Druryan, P. Etwarrow, T. Ferede, M. Fox, D. Gaffen, J. Glascoe, H. Gordon, S. Hollandsworth, X. Jiang, C. Johnson, N. Lawrence, J. Lean, J. Lerner, K. Lo, J. Logan, A. Lueckett, M.P. McCormick, R. McPeters, R.L. Miller, P. Minnis, I. Ramberran, G. Russell, P. Russell, P. Stone, I. Tegen, S. Thomas, L. Thomason, A. Thompson, J. Wilder, R. Willson, and J. Zawodny, 1997: Forcings and chaos in interannual to decadal climate change. *J. Geophys. Res.* **102**, 25679–25720, doi:10.1029/97JD01495.
- Hasselmann, K., 1976: Stochastic climate models 1: Theory. *Tellus*, **28**, 473–485.
- Kara, A.B., P.A. Rochford, and H.E. Hurlburt, 2003: Mixed layer depth variability over the global ocean. *J. Geophys. Res.*, **108** (C3), doi:10.1029/2000JC000736.
- Kiehl, J.T., J.J. Hack, G.B. Bonan, B.A. Boville, D.L. Williamson, and P.J. Rasch, 1998: The National Center for Atmospheric Research Community Climate Model: CCM3. *J. Climate*, **11**,

1131–1149.

Klein, S.A., B.J. Soden, and N.-C. Lau, 1999: Remote sea surface temperature variations during ENSO: evidence for a tropical atmospheric bridge. *J. Climate*, **12**, 917–932.

Kushnir, Y., W.A. Robinson, I. Blade, N.M.J. Hall, S. Pend, and R. Sutton, 2002: Atmospheric GCM response to extratropical SST anomalies: Synthesis and evaluation. *J. Climate*, **15**, 2233–2256.

Maloney, E.D., and A.H. Sobel, 2004: Surface fluxes and ocean coupling in the tropical intraseasonal oscillation. *J. Climate*, **17**, 4368–4386.

Marotzke, J. and D.W. Pierce, 1997: On spatial scales and lifetimes of SST anomalies beneath a diffusive atmosphere. *J. Geophys. Ocean.*, **27**, 133–139.

Marshall, J., Y. Kushnir, D. Battisti, P. Chang, A. Czaja, R. Dickson, J. Hurrell, M. McCartney, R. Saravanan, and M. Visbeck, 2001: North Atlantic climate variability: Phenomena, impacts and mechanisms. *Int. J. Climatol.*, **21**, 1863–1898.

Munnich, M., M. Latif, S. Venzke and E. Maier-Reimer, 1998: Decadal oscillations in a simple coupled model. *J. Climate*, **11**, 3309–3319.

Neelin, J.D., D.S. Battisti, A.C. Hirst, F.-F. Jin, Y. Wakata, T. Yamagata, and S. E. Zebiak, 1998: ENSO theory. *J. Geophys. Res.*, **103**, 14261–14290.

Neelin, J.D., and N. Zeng, 2000: A quasi-equilibrium tropical circulation model—formulation. *J. Atmos. Sci.*, **57**, 1741–1766.

Neelin, J.D., and H. Su, 2005: Moist teleconnection mechanisms for the tropical South American and Atlantic sector. *J. Climate*, **18**, 3928–3950.

Neelin, J.D., and W. Weng, 1999: Analytical prototypes for ocean-atmosphere interaction at mid-latitudes. Part I: coupled feedbacks as sea surface temperature dependent stochastic forcing *J. Climate*, **12**, 697–721.

Nilsson, J., 2000: Propagation, diffusion, and decay of SST anomalies beneath an advective atmosphere *J. Geophys. Ocean.*, **30**, 1505–1513.

- Park, S., C. Deser, and M.A. Alexander, 2005: Estimation of the surface heat flux response to sea surface temperature anomalies over the global oceans. *J. Climate*, **18**, 4582–4599.
- Philander, S. G. H., T. Yamagata and R. C. Pacanowski, 1984: Unstable air-sea interactions in the tropics. *J. Atmos. Sci.*, **41**, 604–613.
- Saravanan, R. and P. Chang, 2000: Interaction between tropical Atlantic variability and the El Niño-Southern Oscillation. *J. Climate*, **13**, 2177–2194.
- Schopf, P.S., 1985: Modeling tropical sea-surface temperature: Implication of various atmospheric responses. *Coupled Ocean-Atmosphere Models*, J. C. J. Nihoul, Ed., Elsevier, 727–734.
- Sobel, A.H. and H. Gildor, 2003: A simple time-dependent model of SST hot spots. *J. Climate*, **16**, 3978–3992.
- Sobel, A.H., I.M. Held, and C.S. Bretherton, 2002: The ENSO signal in tropical tropospheric temperature. *J. Climate*, **15**, 2702–2706.
- Su, H., J.D. Neelin, and J.E. Meyerson, 2005: Mechanisms for lagged atmospheric response to ENSO SST forcing. *J. Climate*, **18**, 4195–4215.
- Tang, B.H., and J.D. Neelin, 2004: ENSO influence on Atlantic hurricanes via tropospheric warming. *Geophys. Res. Lett.*, **31**, L24204, doi:10.1029/2004GL021072.
- Timlin, M.S., M.A. Alexander, and C. Deser, 2002: On the re-emergence of North Atlantic SST anomalies. *J. Climate*, **15**, 2707–2712.
- Watanabe, M. and M. Kimoto, 2000: On the persistence of decadal SST anomalies in the North Atlantic. *J. Climate*, **13**, 3017–30028.
- Wu Z.-X., and R.E. Newell, 1998: Influence of sea surface temperatures on air temperatures in the tropics. *Clim. Dyn.*, **14**, 275–290.
- Zeng, N., J.D. Neelin, and C. Chou, 2000: A quasi-equilibrium tropical circulation model—implementation and simulation. *J. Atmos. Sci.*, **57**, 1767–1796.
- Zhang C.D., M. Dong, S. Gualdi, H.H. Hendon, E.D. Maloney, A. Marshall, K.R. Sperber, W.Q. Wang, 2006: Simulations of the Madden-Julian oscillation in four pairs of coupled and uncou-

pled global models. *Clim. Dyn.*, **27**, 573–592.

TABLE 1: Eigenmode properties for the $N = 5$ basis region decomposition. Values tabulated are modal decay times (days), spatial averages of eigenvectors, and spatial standard deviations of eigenvectors. For complex modes, period is in parentheses beside decay time. Local decay times from the diagonal elements of the sensitivity matrix \mathbf{G} for the 5 regions are: 372.2 (SH EXT), 177.0 (PAC), 146.8 (NH EXT), 127.6 (ATL), 101.6 (IND).

Eigenmode	Decay Time	Spatial Average	Standard Deviation
1	510.3	0.40	0.23
2	260.1	0.21	0.44
3	126.8	0.12	0.48
4	102.1 (4244.7)	0.09-0.06i	0.48
5	102.1 (4244.7)	0.09+0.06i	0.48

TABLE 2: Flux sensitivity parameters.

Symbol	Value
a	0.66
b	3.17
γ	3.5 K K^{-1}
ϵ_H	$5.97 \text{ W m}^{-2} \text{ K}^{-1}$
ϵ_T^{surf}	$-2.81 \text{ W m}^{-2} \text{ K}^{-1}$
ϵ_q^{surf}	$-8.21 \text{ W m}^{-2} \text{ K}^{-1}$
$\epsilon_{T_s}^{surf}$	$6.28 \text{ W m}^{-2} \text{ K}^{-1}$
ϵ_T^{toa}	$2.91 \text{ W m}^{-2} \text{ K}^{-1}$
ϵ_q^{toa}	$-2.55 \text{ W m}^{-2} \text{ K}^{-1}$
$\epsilon_{T_s}^{toa}$	$0.54 \text{ W m}^{-2} \text{ K}^{-1}$

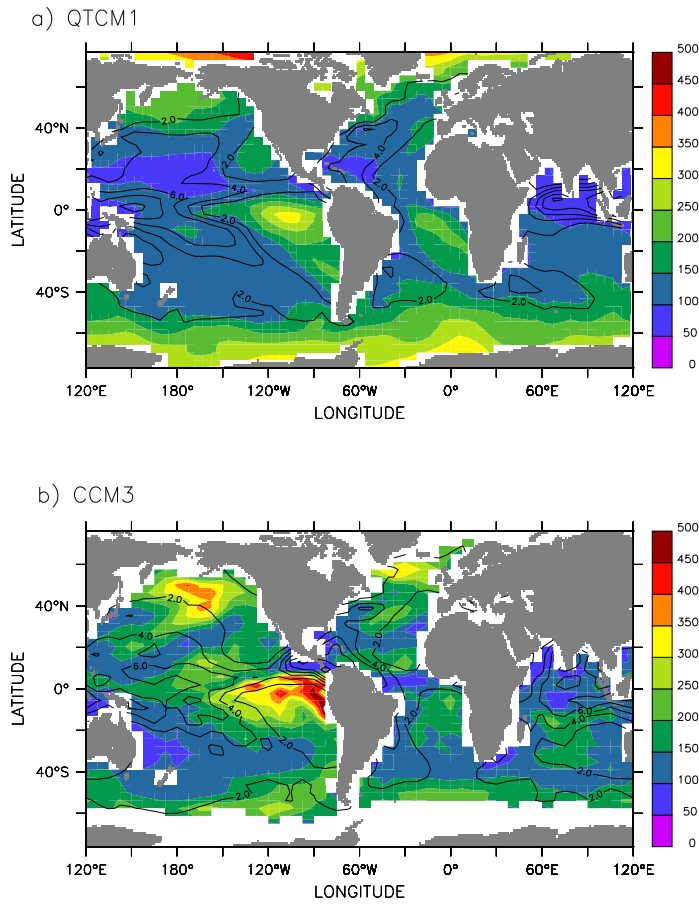


FIGURE 1: Lagged autocorrelation persistence times (in days) for 50 m global mixed layer simulations of QTCM1 (a) and CCM3 (b). Values plotted correspond to the time for the autocorrelation function to fall to e^{-1} . Also shown are contours of time-mean precipitation, in units of mm day^{-1} .

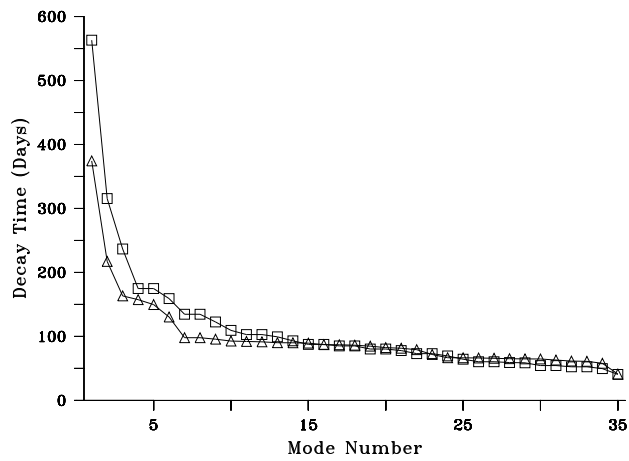


FIGURE 2: Eigenmode decay times for the $N = 35$ basis region eigenvalue analysis. Eigenmode decay times (in days) are plotted as squares. For comparison, local decay times, estimated from the diagonal entries of the flux sensitivity matrix \mathbf{G} , are also shown (triangles).

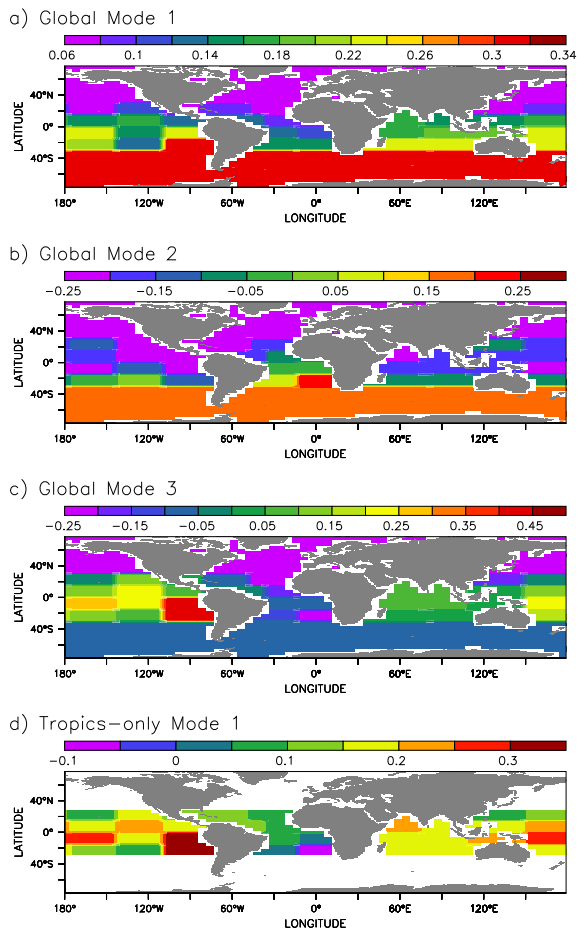


FIGURE 3: Eigenmode spatial loadings of the (a) first, (b) second, and (c) third eigenmodes of the $N = 35$ eigenvalue analysis and (d) the first eigenmode of the tropics-only ($N = 33$) case. Note the difference in color bars between panels; in (a), all values are positive.

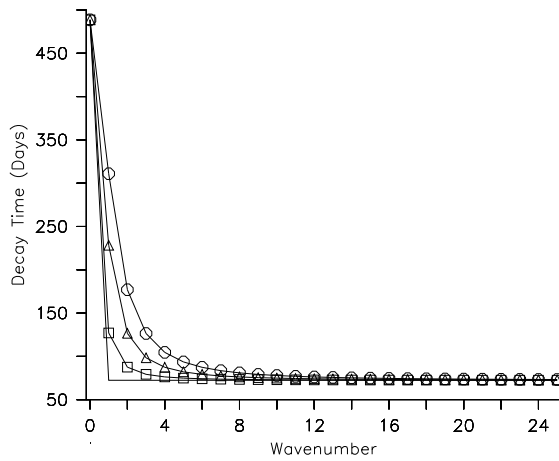


FIGURE 4: Decay time dispersion relationship for the continuous 1D steady-state model. Shown are results for values of the inverse damping length wavenumber k_0 of 0 (no symbols), 1 (squares), 2 (triangles), and 3 (circles). Note that the dispersion curve for values representative of the tropics lies between $k_0 = 1$ and $k_0 = 2$ curves.

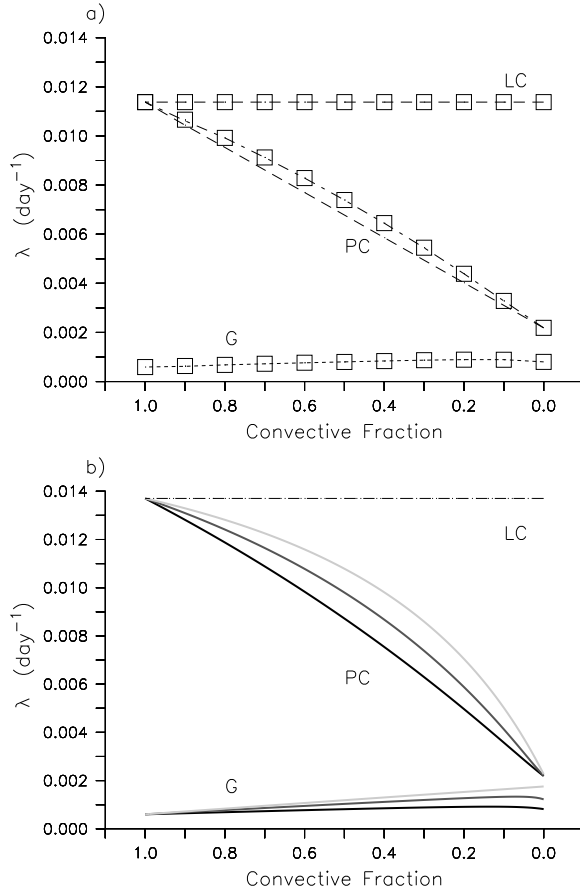


FIGURE 5: Eigenvalues for (a) numerical N-box and (b) analytic 2-box models as a function of the convective fraction α_c in the reduced convective region. In (a), results are for $N = 4$ and $N = 8$ boxes (squares and dashed lines, respectively) for $f_1=0.75$. In (b), results are for $f_1 = 0.75$ (black); 0.5 (dark gray); and 0.33 (light gray). The labels “G”, “PC”, and “LC” denote global decay mode, the mode(s) associated with the partially convecting region, and the local decay modes in the fully convecting region, respectively. In (a), the LC modes are $N - 2$ degenerate and the PC modes are singly- or doubly-degenerate for $N = 4$ and $N = 8$, respectively. In (b), the LC modes are computed from the 2-box model with $\alpha_c = 1$, i.e., the entire tropics is fully convecting.

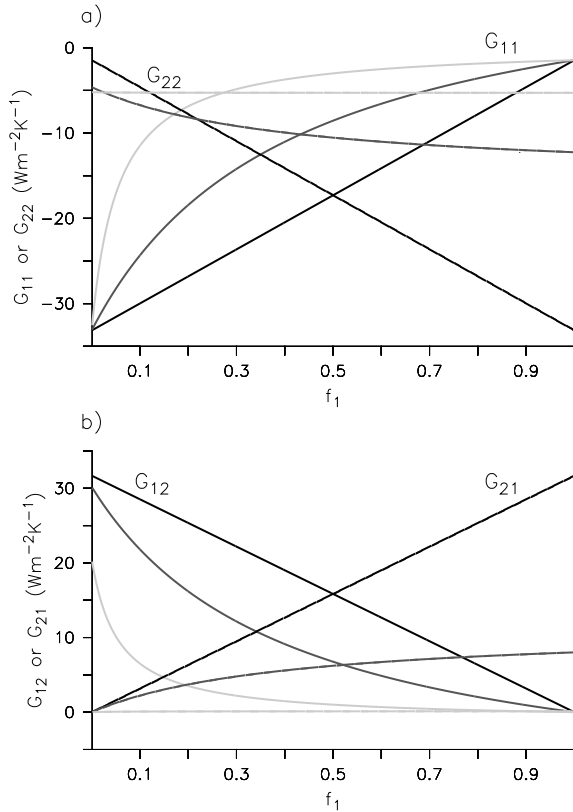


FIGURE 6: (a) Diagonal and (b) off-diagonal matrix elements of \mathbf{G} for the analytic 2-box model as a function of box 1 area fraction f_1 . Solid (dashed) lines in each panel denote G_{11} or G_{12} (G_{22} or G_{21}). Black, dark gray, and light gray lines correspond to box 2 convective fraction values α_c of 1.0, 0.25, and 0.0, respectively. The diagonal elements give the local decay tendencies in the fully convecting and partially convecting regions, respectively; G_{21} gives the effect of SST in the convecting region on surface flux in the reduced-convection region, while G_{12} gives the (typically much smaller) converse.

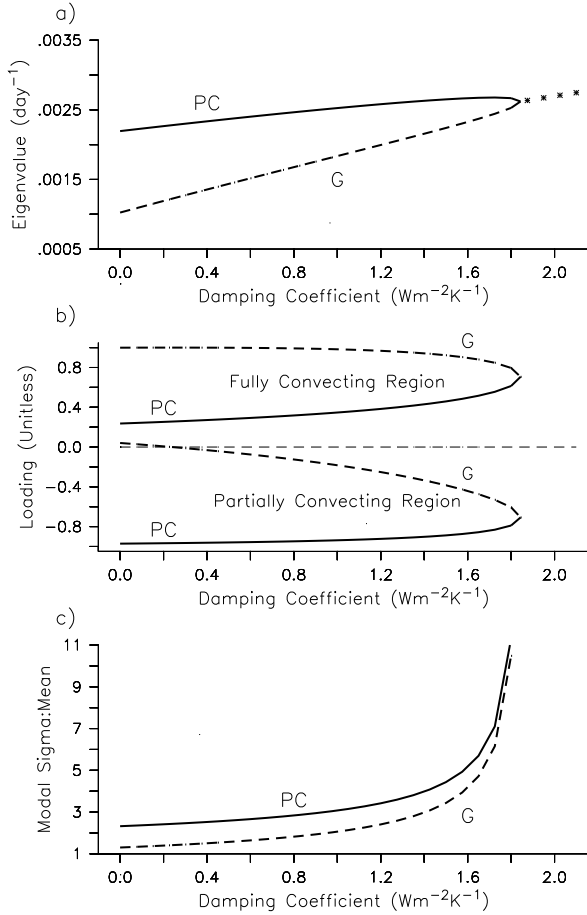


FIGURE 7: Eigenmode properties as a function of horizontal transport/damping coefficients ϵ_T^{tr} and ϵ_q^{tr} . The case shown corresponds to $f_1=0.6$ and $\alpha_c = 0$, i.e., the partially convecting region is nonconvecting, with $\epsilon_T^{tr} = \epsilon_q^{tr}$. Panel (a) illustrates eigenvalues (in units of day^{-1}) for the partially convecting (PC) mode (solid line) and global (G) mode (dashed line). Note that for values of coefficients exceeding $1.84 \text{ Wm}^{-2}\text{K}^{-1}$, the eigenvalues comprise a complex conjugate pair. (b) shows eigenvalue loadings for the two modes in the fully convecting region (top 2 curves) and the partially convecting region (bottom 2 curves), and (c) illustrates ratios of eigenvector standard deviations to eigenvector means for the two modes.

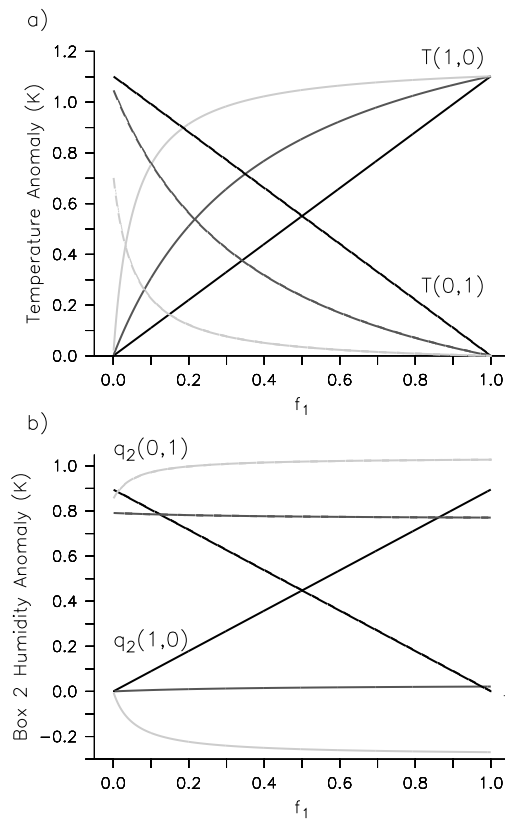


FIGURE 8: (a) Tropospheric temperature and (b) box 2 humidity anomalies for the analytic 2-box model as a function of box 1 area fraction f_1 . Solid lines are for an imposed 1K SST perturbation in box 1 (the fully convecting region), and dashed lines are for an imposed 1K SST perturbation in box 2 (the partially convecting region). Black, dark gray, and light gray lines correspond to box 2 convective fraction values α_c of 1.0, 0.25, and 0.0, respectively.